

## 2 Fundamentals

In this chapter the main experimental techniques used for the thesis at hand are introduced with a focus on X-ray standing wave (XSW) absorption. Besides an introduction to scanning tunneling microscopy (STM) and spectroscopy (STS), angle-resolved photoemission spectroscopy (ARPES) is briefly described with an emphasis on its complementarity to STS. The combination of both techniques allows for detailed studies of the electronic structure of the surface. For further techniques that are used in this work – in this case X-ray photoemission spectroscopy (XPS) and low energy electron diffraction (LEED) – it is e.g. referred to [36,38]. In the last section of this chapter the different experimental setups are described and information on the sample preparation is given.

### 2.1 X-ray standing wave absorption

In this work X-ray standing wave (XSW) absorption was used to gain information on distances between molecular adsorbates and the surface of the underlying substrate with high accuracy (the typical error in this work is in the order of  $0.05\text{\AA}$ ). With this technique not only the distance (or height) of an adsorbate but the heights of different chemical species making up the adsorbate can be determined. However, as XSW is a laterally averaging technique a reasonable order of the adsorbate with respect to the parameters under investigation (height and possibly the lateral position) is necessary.

This section is based on the reviews by J. Zegenhagen [39] and D.P. Woodruff [40] that include beside experimental issues a detailed theoretical background. After a very brief introduction to the basic theoretical ideas this section will concentrate on how the data analysis is carried out.

The basic principle of XSW is shown in Figure 2.1. If a single crystal is irradiated with X-ray photons whose energy matches a Bragg condition the superposition of incident and reflected beam results in a standing wave field (Fig. 2.1.a). The phase difference between incident and reflected beam can be tuned by tuning the photon energy in a small range around the Bragg energy (here:  $\pm 2\text{ eV}$ ) (Fig. 2.1.c). This means that the nodes and antinodes of the standing wave field will move (arrow in Figure 2.1.a). Thus, the intensity of the standing wave field depends on both the height  $h_G$ <sup>1</sup> (of the adsorbate where the intensity is measured) and the photon energy. Therefore for each height (mod  $d_G$ )<sup>2</sup> a unique function (intensity vs. photon energy)

---

<sup>1</sup>The index  $G$ , e.g.  $G = (111)$ , specifies the Bragg planes that are used to form the standing wave field.

<sup>2</sup>The distance between neighboring Bragg planes  $d_G$  corresponds to the periodicity of the intensity of the standing wave field. Thus the functions (intensity vs. photon energy) are identical for

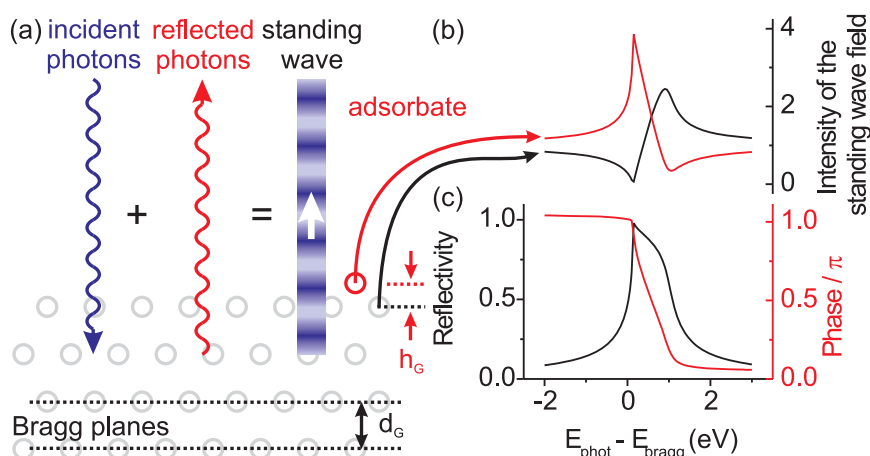


**Figure 2.1:** Basic idea of XSW. a) The superposition of incident and reflected beam creates a standing wave field at an energy that matches a Bragg condition. b) Intensity (normalized by the intensity of the incident beam) of the standing wave field vs. photon energy at two different heights. Beyond the Bragg condition the normalized intensity approximates the expected value 1. c) Reflectivity and phase difference between incident and reflected beam vs. photon energy.

is obtained as illustrated in Figure 2.1.b. The experimental goal is the determination of these functions (the intensity profiles in Fig. 2.1.b) which are used to calculate the heights of the adsorbates. These intensity profiles are determined indirectly by measuring the photoelectrons that are emitted by the adsorbate in a setup for X-ray photoemission spectroscopy (XPS). This approach makes sense because the photoelectron yield of the core-levels of an adsorbate directly depends on the intensity of the standing wave field at the adsorbate position. Moreover, this approach includes the above-mentioned possibility of determining the height  $h_G$  of each chemical species of the adsorbate.

In the following this section will focus on normal incidence XSW (NIXSW). For NIXSW the X-ray beam is perpendicular to the Bragg planes, i.e. the Bragg condition is met at a Bragg angle of close to  $90^\circ$ .<sup>3</sup> An important prerequisite for performing NIXSW measurements is the possibility to tune the photon energy to meet the Bragg condition. Thus, synchrotron radiation is necessary. By using different Bragg planes it is in principle possible to triangulate the position of the adsorbate, i.e. to determine beside the height also the lateral position with respect to the underlying substrate.

It is noted that instead of tuning the photon energy changing the angle between sample and X-ray beam basically results in the same effect of traversing the Bragg condition. In this way the first successful XSW measurements were carried out. In this case the Bragg condition is met in an off-normal setup and thus laboratory X-ray

all heights  $h_G + n \cdot d_G$  ( $n \in \mathbb{N}$ ) and the determined height of an adsorbate always contains the undefined offset  $n \cdot d_G$ .

<sup>3</sup>Depending on the Bragg planes that are used NIXSW does not necessarily imply that the X-ray beam is perpendicular to the surface.

sources can be used whose energy cannot be tuned. However, such an approach makes high demands on both the experimental setup (angles have to be tuned in a range significantly smaller than  $1^\circ$ ) and the quality of the crystal (small mosaicity). To a certain extent these constraints are overcome with NIXSW as the width of the curves (Fig. 2.1.b and c) exhibit a maximum at a Bragg angle of  $90^\circ$ .

### 2.1.1 X-ray diffraction

In the introduction it is already indicated that a detailed knowledge on the quantitative behavior of the standing wave field with respect to the photon energy and the height  $h_G$  is necessary to calculate the latter value. For this purpose theories on X-ray diffraction are used. A very well known approach is the *kinematical theory of (X-ray) diffraction* in which an incoming plane wave interferes with spherical waves arising from each point (atom) of the crystal under study. This interference is calculated at a distance that is large compared to the dimensions of the crystal. Including the periodicity of the crystal lattice and the information on its basis, the determination of both the Laue condition which is equivalent to the Bragg condition and the structure factor which describes the relative “intensity of the Bragg points” is possible. One drawback of this approach is the negligence of the extinction of the incoming plane wave: A spherical wave that departs from the inside of the crystal has the same weight as a wave departing from an equivalent position of its surface. Moreover, each atom “generates” only one spherical wave. Thus, multiple scattering events are neglected.

The constraints of the *kinematical theory of (X-ray) diffraction* are overcome in the theory of *dynamic (X-ray) diffraction* which allows an accurate description of the diffraction at the crystal. Within this theory the intensity of the wave field at a specific height  $h_G$  and at an energy  $E$  is:

$$I_G^{\text{WF}}(h_G, E) = 1 + R(E) + 2 \cdot \sqrt{R(E)} \cdot \cos\left(\nu(E) - 2\pi \frac{h_G}{d_G}\right) \quad (2.1)$$

- $I_G^{\text{WF}}$  Intensity of the (standing) wave field (WF) normalized by the intensity of the incident beam (cf. Fig. 2.1.b)
- $R(E)$  Reflectivity (cf. Fig. 2.1.c)
- $\nu(E)$  Phase between the incident and reflected beam (cf. Fig. 2.1.c).

The reflectivity and the phase can be extracted from the ratio of the electric fields:

$$\frac{\mathcal{E}_G(E)}{\mathcal{E}_0(E)} = \sqrt{R(E)} \cdot e^{i\nu(E)} \quad (2.2)$$

- $\mathcal{E}_G$  Electric field of the wave reflected at the Bragg planes characterized by G
- $\mathcal{E}_0$  Electric field of the incident wave.

As the reflectivity approximates 0 outside the Bragg condition (Fig. 2.1.c) the normalized intensity of the wave field approximates 1 (Equation 2.1). In other words:

Outside the Bragg condition the intensity of the wave field corresponds to the intensity of the incident wave and the standing wave field ceases to exist. If the energy dependent intensity at the position of the adsorbate is known Equation 2.1 can be used to fit this curve with the parameter  $h_G$ .

### 2.1.2 Relation between the intensity of the standing wave field and the photoelectron yield

The intensity of the standing wave field at the adsorbate position is determined indirectly by measuring the photoelectron yield for the core levels of the different chemical species making up the adsorbate. In first order the intensity of the standing wave field is assumed to be proportional to the photoelectron yield, i.e. the intensity (area) of the XPS peak. However, XPS measures the signal of every element (of the same chemical species) with the (probably varying) height  $h_{G,i}$ . The XPS intensity at a photon energy  $E$  should then be proportional to the sum of the intensities  $I_G^{\text{WF}}(h_{G,i}, E)$  at the element positions  $h_{G,i}$ :

$$I_G^{\text{XPS}}(E) \propto \sum_i I_G^{\text{WF}}(h_{G,i}, E) \quad (2.3)$$

$I_G^{\text{XPS}}(E)$	Intensity of an XPS core level peak measured at the photon energy $E$
$I_G^{\text{WF}}(h_{G,i}, E)$	Intensity of the standing wave field at the position of element $i$ (cf. Eq. 2.1).

The sum of the *cos*-terms in Equation 2.3 (cf. Equation 2.1) containing the same variable  $\nu$  but different phases  $2\pi \cdot h_{G,i}/d_G$  results in a *cos*-term with a new phase  $\bar{h}_G$  and a new amplitude  $F_G$ . The XPS signal is then proportional to:

$$I_G^{\text{XPS}}(E) \propto 1 + R(E) + 2 \cdot \sqrt{R(E)} \cdot F_G \cdot \cos(\nu(E) - 2\pi P_G) \quad (2.4)$$

$F_G$	Coherent fraction
$P_G$	Coherent position: $P_G = \bar{h}_G/d_G$ .

The coherent fraction  $F_G$  indicates the disorder<sup>4</sup> of the element that is studied. A coherent fraction of 1 indicates a perfect order, i.e. every element adsorbs at the same height whereas a decreasing coherent fraction indicates increasing disorder.

Until now a proportionality between the intensity of the standing wave field and the photoelectron yield was assumed. This approximation is valid as long as the wave length of the wave field significantly exceeds the dimensions of the atom. In the experiments described in this work the X-ray wavelength is 4.3 Å. Thus, deviations from this so called dipole approximation have to be taken into account. This becomes even more important if the electron distribution of an atom is asymmetric since the

---

<sup>4</sup>This disorder only refers to the axis perpendicular to the Bragg plane  $G$ , i.e. varying heights  $h_{G,i}$  of the element  $i$  induce disorder.

**Table 2.1:** Quadrupole parameters on Cu(111) taken from [42].

	Carbon(1s)	Nitrogen(1s)
$S_R$	1.76	1.77
$ S_I $	1.382	1.388
$\Psi$	-0.055	-0.067

reflected wave might be absorbed in a different way than the incident wave. These deviations are accounted for as quadrupole parameters  $S_R$  and  $S_I$  that are included in Equation 2.4 in the following way:

$$I_G^{\text{XPS}}(E) \propto 1 + R(E) \cdot S_R + 2 \cdot \sqrt{R(E)} \cdot |S_I| \cdot F_G \cdot \cos(\nu(E) - 2\pi P_G + \Psi) \quad (2.5)$$

$$S_I = |S_I| \cdot e^{i\Psi}$$

The parameter  $S_I$  is a complex number with absolute value  $|S_I|$  and phase  $\Psi$ . It is noted that another parametrization of these non-dipolar contributions exists which, however, is used less in literature. It was introduced by Nelson et al. [41] and consists of the two independent parameters  $q$  and  $\Delta$ . The quadrupole parameters normally depend on the experimental geometry, the element number, the photon energy and the orbital symmetry of the initial state. For the analysis presented in this thesis the quadrupole parameters (Table 2.1) were taken from [42] where they were determined for NIXSW measurements on Cu(111).

The energy dependent photoelectron intensity  $I_G^{\text{XPS}}(E)$  (Eq. 2.5) of a specific element is called *photoelectron yield curve* in the following. Each value of the photoelectron yield curve at photon energy  $E$  represents the intensity of a core-level peak (XPS-spectrum) taken with photon energy  $E$ .

### 2.1.3 Data analysis with DARE

Together with the reflectivity (Fig. 2.1) which is called *rocking curve* in the following, the photoelectron yield curve (Equation 2.5) is used to determine coherent fraction and position. For this procedure the software DARE developed by J. Zegenhagen is used. In the following the basic concept of the software is described with emphasis on several aspects which are relevant for the analysis of the experimental data presented in this work.

In a first step, DARE recalibrates the energy scale and the intensity scale of the rocking curve to determine the energy-dependent behavior of the reflectivity  $R(E)$  and the phase  $\nu(E)$ . This is done after subtracting an offset. This is reasonable as the reflectivity is supposed to approximate 0 outside the Bragg condition. Deviations of the experimental photon energy scale from the theoretically determined scale may be due to both monochromator drift and the not negligible mosaicity of the crystal.

In a second step, the information on reflectivity and phase are used to fit the photoelectron yield curve and to extract coherent fraction and phase. Because the diffraction of the crystal is already fully characterized after the first step the fit of the photoelectron yield curve is an unambiguous (non-critical) process with respect to the fit parameters: Either the fit works and coherent fraction and position are determined or the curve cannot be described by the theoretical model. Thus, the most critical step is the fit of the rocking curve. Because of this, the rest of the paragraph is dedicated to the effects of monochromator drift and mosaicity of the crystal that both influence the rocking curve.

For performing XSW measurements a photon energy just below the Bragg condition is used as initial value. After recording the relevant XPS spectra the energy is increased a bit and the recording of the XPS spectra is repeated at the new photon energy.

The experimental setup used for this work exhibited a noticeable monochromator drift. Thus, in order to reduce the monochromator drift (backlash) a photon energy lower than the initial value was chosen. By this the (real) initial value for the XSW experiment was stepwise approached from below. The residual drift should result in a deviation of the theoretical energy range from the experimental one whereas the intensity should not be affected.

In [43] real and thus imperfect crystals are considered as a conglomeration of tiny, perfect crystals (mosaic blocks) which have slightly different orientations. There, mosaicity is defined as the “width of the distribution of mis-orientation angles of all the unit cells in a crystal”. Each mosaic block matches the Bragg condition at a slightly different photon energy. In principle each mosaic block provides its own rocking curve which is shifted on the photon energy scale compared to the rocking curves of other mosaic blocks. Summing up all individual rocking curves thus leads to a broadened rocking curve. Its intensity in comparison to a rocking curve of a crystal without mosaicity is lower. Hence, for occurring mosaicity the energy range of the rocking curve determined by DARE is narrowed compared to the energy range used in the experiments. DARE can mimic mosaicity to a certain extent by artificially increasing the divergence of the photon beam which is caused by the monochromator and described through the asymmetry parameter  $b$ . This divergence can be adjusted such that the two energy ranges mentioned above agree with each other.

While monochromator drift should result in rocking curves of identical intensity but different width the experimental data within this work exhibit two different features: Rocking curves taken at different positions on the same sample differ in peak position, intensity and width (Fig. 2.2.c). However, some curves are nearly identical (Fig. 2.2.d). Thus, the dominating influence on the rocking curve results from mosaicity which is therefore taken into account in the XSW analysis of this work. However, it is important to note how the “consideration” of mosaicity affects coherent fraction and position. This is shown in Fig. 2.2.a and b. The addition of mosaicity involves an average systematic deviation of -0.1 for the coherent fraction and an increase of height of  $0.01 \text{ \AA}$  for the adsorbate. Especially the latter deviation does not exceed the typical error of the coherent positions determined in this work. Hence, neither monochromator drift nor mosaicity seem to lead to significant errors in our case.

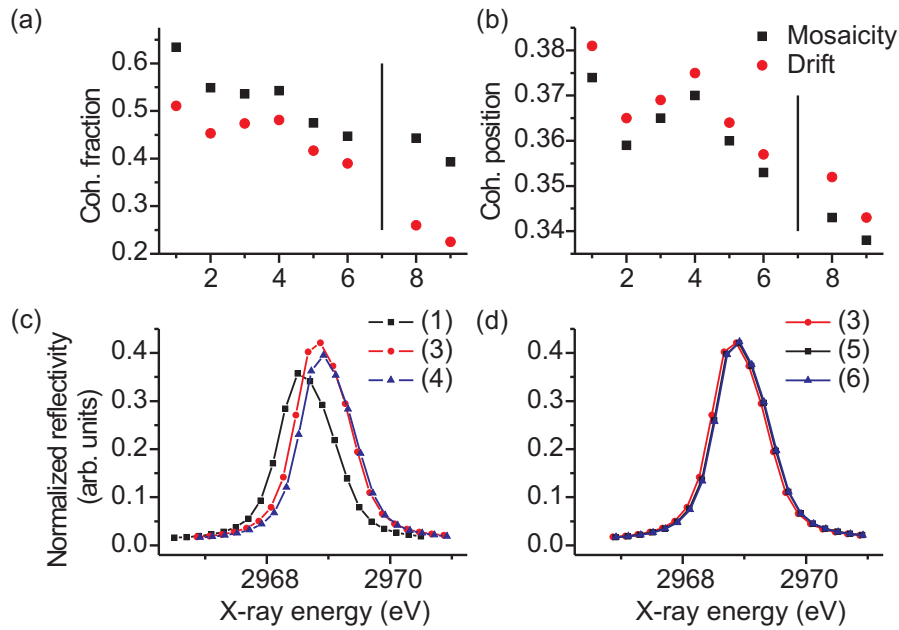


**Figure 2.2:** Coherent fraction (a), coherent position (b) and rocking curves (c, d) determined at different positions on two Cu(111) crystals (labeled from 1 to 9). The coherent position and fraction are determined for the N1s peak of the NH group of the perylene derivative DPDI forming a disordered assembly on the surface (Section 5.1). The positions 1–6 refer to one crystal whereas 8 and 9 refer to a another one.

### 2.1.4 XPS analysis

In order to determine a photoelectron yield curve, which is used as input for DARE (cf. Section 2.1.3), a set of XPS spectra taken with different photon energies has to be analyzed. The task is to calculate the peak intensity of each spectrum which can be done in two ways: The XPS spectra are either first fitted and subsequently, the area of the peak is calculated from the fit or the area is directly determined from the measured data. The advantage of the latter method is its simplicity because no assumptions are made e.g. for the shape of the peak. However, a fit may be necessary if two peaks are close to each other, i.e. if the peak positions for the same element within different chemical environments only differ by a few eV. This is the case for the experiments presented in this work. In order to have “comparable errors” the fitting strategy is always used, whether necessary or not.

Figure 2.3 compares both strategies for a set of XPS spectra of the same chemical species. The coherent positions exhibit a systematic deviation of 0.01 which corresponds to a difference in height of 0.02 Å. For the coherent fraction the choice of one strategy does not seem to induce a systematic error (Fig. 2.3). In the case of the direct determination of the peak area (filled squares in Fig. 2.3), the deviations from the average coherent position seem to be smaller compared to the deviations from the average coherent fraction. Furthermore, the coherent fractions, calculated from the direct determination of the peak area, seem to differ more strongly from the

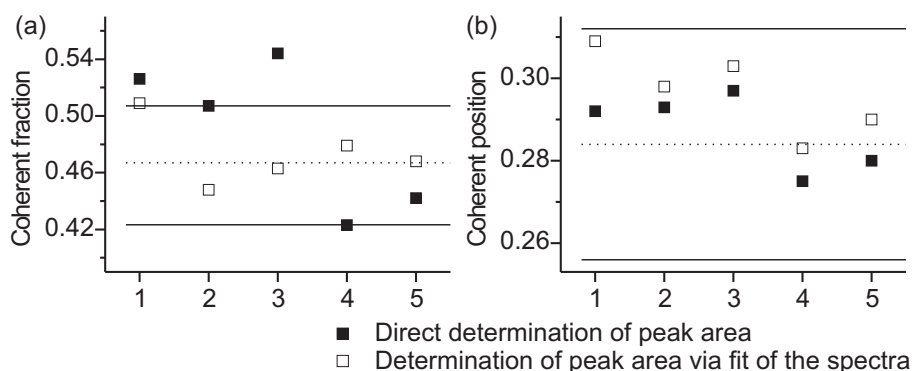


**Figure 2.3:** Coherent fraction (a) and position (b) for five different sample positions. Two strategies were used to analyze the XPS spectra at five different positions on the sample (labeled 1 to 5). For the hollow squares the XPS spectra were fitted and the area of the peak was calculated from the results of the fit whereas for the filled squares the area of the peak was determined directly. The black dotted lines show the average coherent fraction and position, respectively. The straight lines indicate the corresponding standard deviations. These statistical values were obtained by the first strategy and include besides the five positions shown here ten additional positions. Coherent fraction and position are displayed for the C1s peak of the perylene derivative DPDI adsorbed on Cu(111) in a disordered phase (Section 5.1).

average coherent fraction than those whose calculation is based on the fits of the XPS spectra. Although the statistics is not sufficient to make a rule from this observation, it can be qualitatively understood in the following way. While the coherent position is determined by the shape of the photoelectron yield curve the coherent fraction is determined by its deviation from 1. For XPS spectra with low peak intensity (low photoelectron yield) noise might significantly affect the direct determination of the peak area. In contrast, the fit with a fixed peak position and width might result in a noise reduction. Moreover these considerations show the robustness of the XSW technique with respect to the determination of the coherent position, i.e. the height of the adsorbate.

### 2.1.5 The fitting algorithm for the XPS peaks

Due to the massive data acquisition of XPS spectra<sup>5</sup> their analysis has been automatized. The corresponding script has to consider parameters like shake up, linear and/or Shirley background and the peak positions. In general, a large set of adjustable fit parameters creates significant dependencies between these parameters. In the worst case the fitting procedure becomes untrustworthy. Moreover, the fitting procedure is further complicated as beam damage sets an upper limit to the data acquisition time what results in rather noisy XPS spectra (Fig. 2.4.b).

<sup>5</sup>Each photoelectron yield curve is the result of the analysis of approximately 20 XPS curves. Two different assemblies are studied with focus on the N1s and C1s spectra.

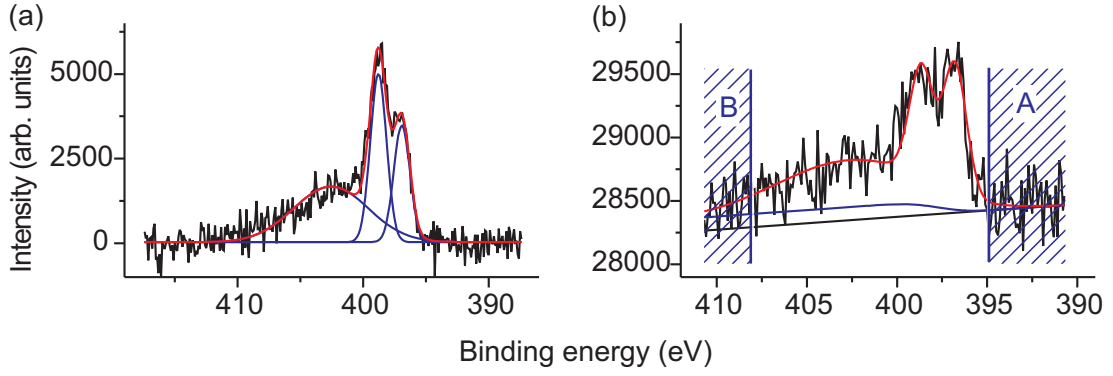


**Figure 2.4:** N1s spectra together with the corresponding fits for submonolayer coverage of DPDI on Cu(111). a) Spectrum recorded with “good” statistics after background subtraction in order to gain reliable information on peak positions and widths. b) Fit of one XPS spectrum that is part of an “XSW-set” (the analysis of the XPS spectra of one set results in one photoelectron yield curve). The effects that are considered by the fitting algorithm are exemplarily illustrated: The overall curve (red) is the sum of the fits of the two N1s peaks and the shake up, the Shirley background (blue) and the linear background (black).

Hence, the aim of an optimized script includes the reduction of the number of adjustable fit parameters. For this reason the peak shape is described by a Gauss profile and not by a perhaps more accurate Voigt profile assuming that the Gauss profile of the analyzer will dominate the peak shape. Thus, the following fit function has been used:

$$\begin{aligned}
 \text{Fit}(E) = & \underbrace{C + L \cdot E}_{\text{Linear background}} + \underbrace{B \cdot \text{shi}_{\tilde{E}, \tilde{w}}(E)}_{\text{Shirley background}} + \\
 & \underbrace{A_{SU} \cdot \exp\left\{-\frac{(E - E_{SU})^2}{2 \cdot w_{SU}^2}\right\}}_{\text{Shake Up}} + \underbrace{A_P \cdot \exp\left\{-\frac{(E - E_P)^2}{2 \cdot w_P^2}\right\}}_{\text{XPS peak}} \quad (2.6) \\
 \text{shi}_{\tilde{E}, \tilde{w}}(E) = & \int_{-\infty}^E \exp\left\{-\frac{(\mathcal{E} - \tilde{E})^2}{\tilde{w}^2}\right\} d\mathcal{E}
 \end{aligned}$$

- |                          |  |
|--------------------------|--|
| $C, L$                   | Offset and slope of the linear background                            |
| $B, A_{SU}, A_P$         | Amplitudes of the Shirley background, the shake up and the peak      |
| $\tilde{E}, E_{SU}, E_P$ | (Peak) energies of the Shirley background, the shake up and the peak |
| $\tilde{w}, w_{SU}, w_P$ | (Peak) widths of the Shirley background, the shake up and the peak.  |